EARTHQUAKES

Nucleation speed limit on remote fluid-induced earthquakes

Tom Parsons,[1]* Luca Malagnini,[2] Aybige Akinci[2]

Earthquakes triggered by other remote seismic events are explained as a response to long-traveling seismic waves that temporarily stress the crust. However, delays of hours or days after seismic waves pass through are reported by several studies, which are difficult to reconcile with the transient stresses imparted by seismic waves. We show that these delays are proportional to magnitude and that nucleation times are best fit to a fluid diffusion process if the governing rupture process involves unlocking a magnitude-dependent critical nucleation zone. It is well established that distant earthquakes can strongly affect the pressure and distribution of crustal pore fluids. Earth's crust contains hydraulically isolated, pressurized compartments in which fluids are contained within low-permeability walls. We know that strong shaking induced by seismic waves from large earthquakes can change the permeability of rocks. Thus, the boundary of a pressurized compartment may see its permeability rise. Previously confined, overpressurized pore fluids may then diffuse away, infiltrate faults, decrease their strength, and induce earthquakes. Magnitude-dependent delays and critical nucleation zone conclusions can also be applied to human-induced earthquakes.

INTRODUCTION

When an earthquake happens spontaneously, it is nearly always accompanied by aftershocks that cluster around it in time and space. Physical explanations for this include static stress transfer, which is caused by permanent distortion of the crust from slip on the mainshock fault plane that can, in turn, trigger more local earthquakes (*1*), as well as dynamic stress transfer, where straining of the crust by seismic waves temporarily changes the stress state long enough to trigger aftershocks (*2*). The aftershock zone stretches much farther than the obvious areas immediately around the mainshock rupture, as evidenced by significant seismicity outbreaks that can be attributed to passing long-period surface waves (high-amplitude seismic waves trapped in Earth's crust) from Earth's largest ($M \geq 7$) mainshocks at global distances (*2*, *3*). Remotely triggered earthquakes [greater than ~300 km away from $M \geq 7$ mainshocks on average (*4*)] can only be initiated by seismic waves, because static stresses become vanishingly small with distance.

Identifying remote dynamically triggered earthquakes is complicated because unrelated, spontaneous earthquakes can coincide with seismic wave arrivals by chance and/or mask their signal (*5*). Nonetheless, many individual studies link seismicity outbreaks, well-water level changes, volcanic activity, and nonvolcanic tremor to mainshock earthquakes that can be on opposite sides of Earth (*6*–*16*). Unequivocal seismicity outbreaks triggered by remote earthquakes are rare (*17*) but can be attributed to about 3% of $M \geq 7.0$ mainshocks worldwide at any given locality (*5*). The possibility that an earthquake that happens on one side of Earth might prompt a second, damaging shock on the opposite side raises obvious concerns. Is there a period of enhanced worldwide seismic hazard that follows every large earthquake? How long might such an alarm last?

Because dynamic earthquake triggering is initiated by seismic wave oscillations that temporarily stress the crust, there is no expected net change after the waves pass through. Intuitively, we would anticipate triggering to occur during this transient period, and many times, this is what happens (*3*). However, observations show that many dynamically triggered earthquakes do not initiate immediately but are instead delayed by hours or days following the passage of surface waves, an effect that is easiest to see among the largest remotely triggered earthquakes (*18*–*22*) because background rates of small earthquakes are the highest. Delayed remote earthquake triggering may be caused by surface waves that circle the globe more than once (*23*), by waves that jostle and change frictional properties in a fault zone (*24*) that causes delayed nucleation (*25*), or by a process where waves shake open (*26*) a fluid pressure valve (*27*) that unlocks a fault.

As an example, we highlight two well-documented (*6*, *7*, *28*) cases of remote dynamic earthquake triggering that struck the Basin and Range Province of the western United States following the 1992 M = 7.4 Landers, CA and 2002 M = 7.9 Denali, AK earthquakes. These cases illustrate (Fig. 1) what regional responses to distant mainshocks look like. They show widely distributed, anomalously high seismicity rates that initiate as surface waves pass through. Their rates rise sharply and then decay over time like aftershocks, although they occur without a local mainshock. These examples demonstrate a globally observed tendency (*5*, *18*–*22*) for remotely triggered sequences to be deficient in higher-magnitude earthquakes during the first 24 hours (or longer) as compared with local aftershocks (Fig. 1), which may be a result of comparatively smaller numbers of remotely triggered events or because of a physical process. The combined remote (r > 300 km) response in the Basin and Range Province shows that most of the triggered M ~ 2 to M ~ 3 shocks happen in the first 24 hours, whereas most of the M ~ 3 to M ~ 4 events happened during the first 30 days (Fig. 1D). Published physical explanations of dynamic triggering modes usually invoke the oscillating deformation of a fault zone by seismic waves that causes transient stress increases that briefly cross a failure threshold (*8*, *9*, *24*, *29*, *30*). Here, we focus on the interval between this temporary stressing of the crust and eventual occurrence of triggered earthquakes because it is diagnostic of their nucleation process.

RESULTS

It is not difficult to identify temporal associations between individual distant earthquakes because Earth produces continuous seismicity in its most active regions, and therefore, any two shocks can be correlated in time. It is more difficult to establish causation and to find clear examples such as those depicted in Fig. 1. We thus work from a

[1]U.S. Geological Survey, MS-999, 345 Middlefield Road, Menlo Park, CA 94025, USA. [2]Istituto Nazionale di Geofisica e Vulcanologia, Via di Vigna Murata 605, Rome, Italy. *Corresponding author. Email: tparsons@usgs.gov

published global compilation of remotely triggered earthquakes that were identified through a systematic process of using high-quality seismic networks (capable of recording and locating earthquakes down to $M \sim 2$) on all continents except Antarctica (*5*). Periods before and after a group of all $M \geq 7.0$ mainshocks that have happened globally since 1979 were checked for anomalous local seismicity outbreaks such as those depicted in Fig. 1. A population of earthquakes recorded within 17 seismograph networks during periods when passing surface waves from 260 $M \geq 7.0$ mainshocks was assembled. We study the most robust of these results, as defined by a rate increase during the 24-hour period after surface waves have passed that is much greater (>2σ) than normal day-to-day variation in both time and space and that is not attributable to any known local cause (Fig. 2). Ultimately, 1249 $M \geq 2$ earthquakes are culled from 34,095 candidate events that have characteristics in common with the most diagnostic behavior of aftershocks, an Omori law (*31*) decay (rate decreases as inverse of time) (Fig. 3), yet they are widespread and have no local mainshocks. Given that their initiation correlates with passing surface waves from remote mainshocks, we find that the most reasonable conclusion is that we have a population of identified, remotely triggered earthquakes for which the nucleation behavior can now be studied.

We are primarily interested in learning more about the largest remotely triggered earthquakes because they are the most dangerous. Indications from past studies suggest that these largest events happen but that they are often delayed relative to the arrival of surface waves (*18*–*22*). We begin by carefully examining the earliest observed events in the population of remotely triggered earthquakes as a function of their magnitudes to establish if there are any consistent patterns. We

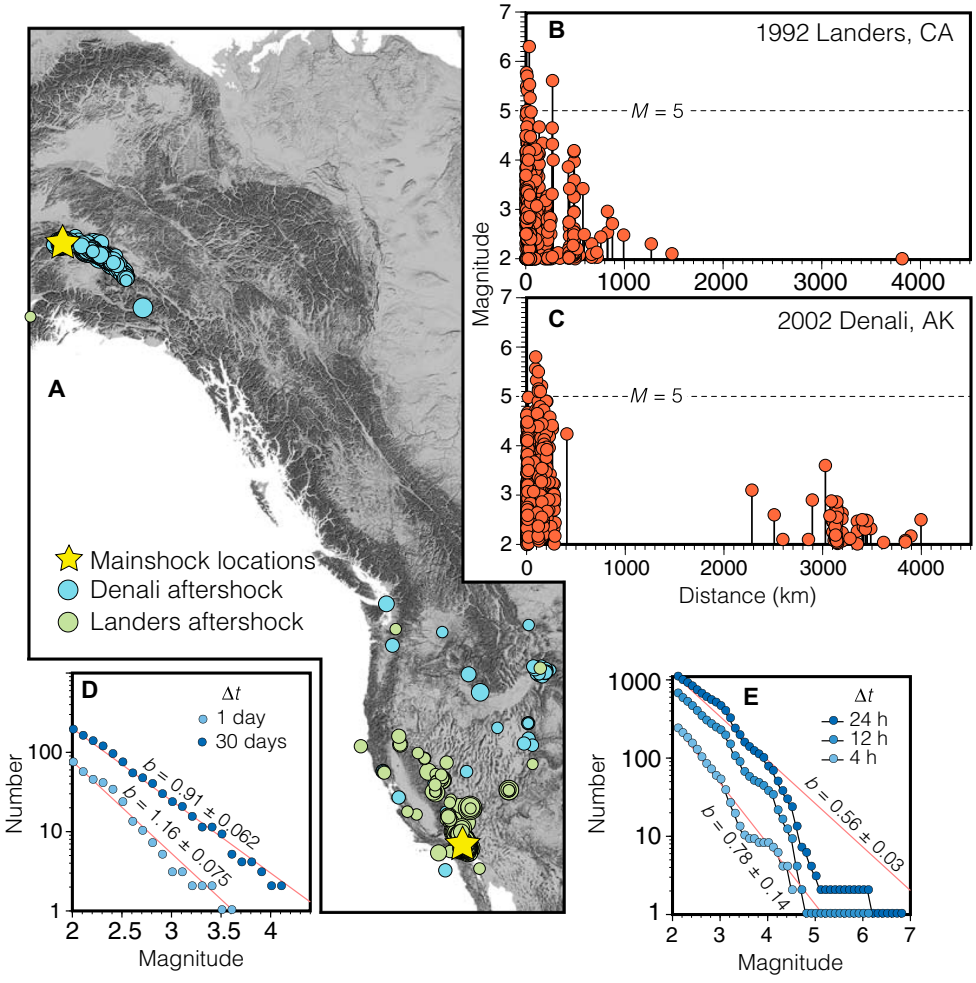

Fig. 1. Examples of known (*6*, *7*, *28*) remote dynamic triggering. (**A**) In the Basin and Range Province of the western United States. All $M \geq 2.0$ western U.S. seismicity during the 24 hours after both the 1992 $M = 7.4$ Landers, CA (green dots) and the 2002 $M = 7.9$ Denali, AK (blue dots) earthquakes are shown. Both earthquakes have abundant local aftershocks and have produced significant triggered seismicity in the Basin and Range Province. Yellow stars show mainshock locations. The magnitude versus distance distribution from (**B**) the Landers earthquake shows continuous aftershocks trending into the Basin and Range Province out to ~1500 km away, whereas the (**C**) Denali earthquake has a clear spatial gap between local and remote aftershocks (~400 to 2300 km). Both earthquakes only have $M \geq 5$ aftershocks within 300 km from mainshocks during the first 24 hours. The cumulative magnitude-frequency distribution of remotely triggered earthquakes in the Basin and Range Province during the first 24 hours after mainshocks is shown in (**D**). It is initially deficient in $M \geq 3.5$ events (lighter blue points), whereas after 30 days [approximate duration of the rate increase (*28*)], it begins to fill in (darker blue dots) as evidenced by a significant decrease in the slope (*b* value) (Methods). Similarly, in (**E**), the temporal evolution of cumulative magnitude-frequency trends is shown for a global compilation (*5*) of remotely triggered earthquakes over 24 hours. The distributions are deficient at higher ($M \geq 4.5$) magnitudes but gradually fill in over time, with *b* values decreasing.

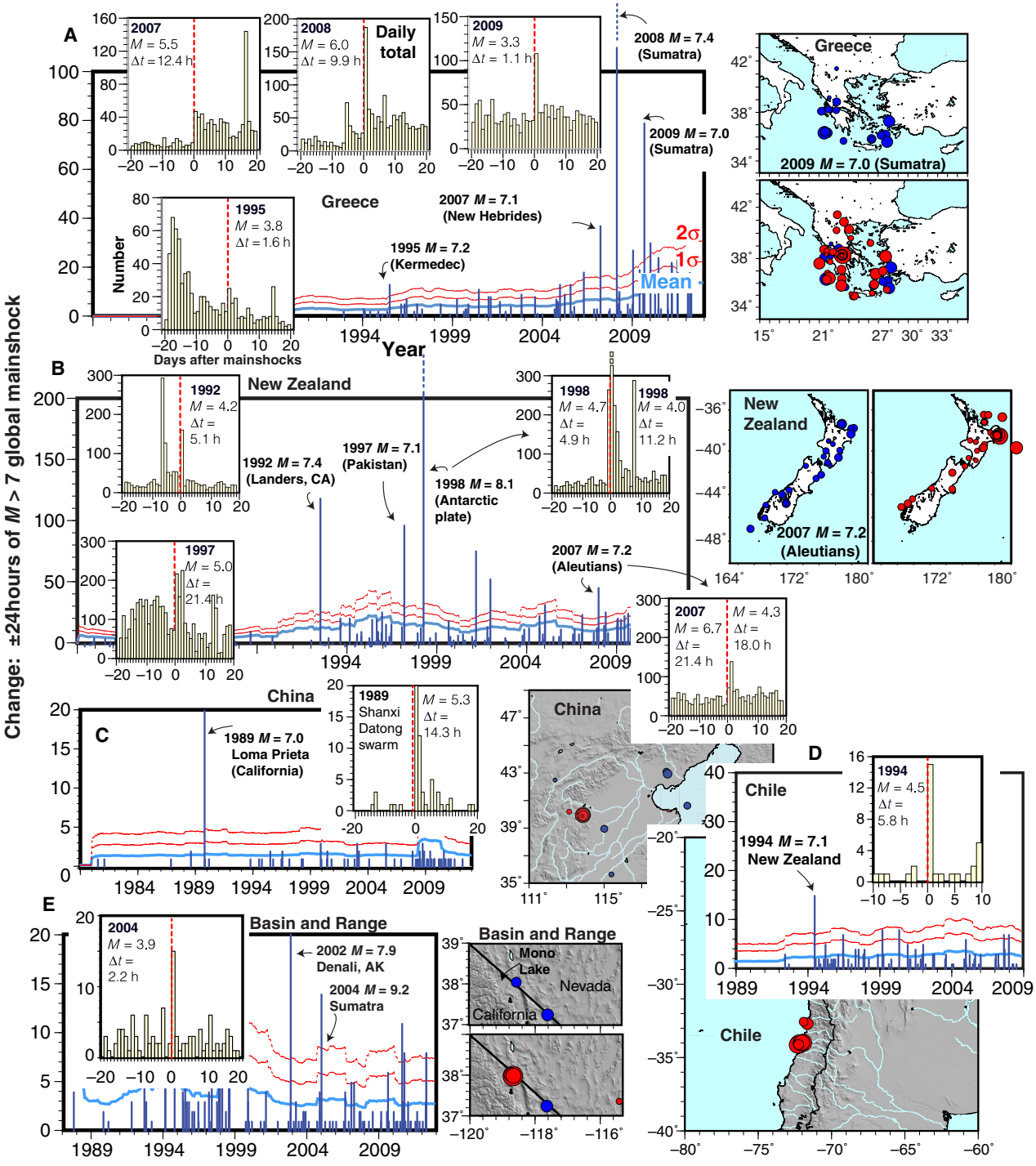

Fig. 2. Examples of the earliest occurrences of remotely triggered earthquakes across the magnitude spectrum worldwide in (**A**) Greece, (**B**) New Zealand, (**C**) China, (**D**) Chile, and (**E**) the Basin and Range Province of the United States. Remotely triggered earthquakes are defined as regional outbreaks occurring at rates significantly (>2σ) greater than day-to-day mean variation within local seismograph networks associated with surface wave arrivals from remote (r > 1000 km) global mainshocks ($M \geq 7.0$). Blue spikes show ±24-hour variation in earthquake rates within regional networks, and red dashed lines show 1σ and 2σ variation on the mean variability (blue curves). Yellow histograms show daily seismicity rates for ±20 days before and after global mainshocks. Example maps show spatial distributions with red dots representing earthquakes in the 24 hours after surface wave arrivals and blue dots showing those in the 24 hours before. These examples demonstrate the origins of the earliest occurrences of $3.0 \leq M \leq 6.7$ triggered earthquakes used to construct the relations shown in Fig. 3. Many more events are detected globally (*5*).

organize the combined catalog of remotely triggered earthquakes by sorting them into 0.1 magnitude-unit bins and then we find the earliest occurrence of events within each bin. These first occurring earthquakes are traced back to their original locations and checked to ensure that they are not examples of secondary triggering, meaning that a smaller nearby event could be responsible for initiating it by static or local dynamic triggering. We plot the geographic and temporal distributions of the earliest and subsequent remotely triggered earthquakes in Fig. 3.

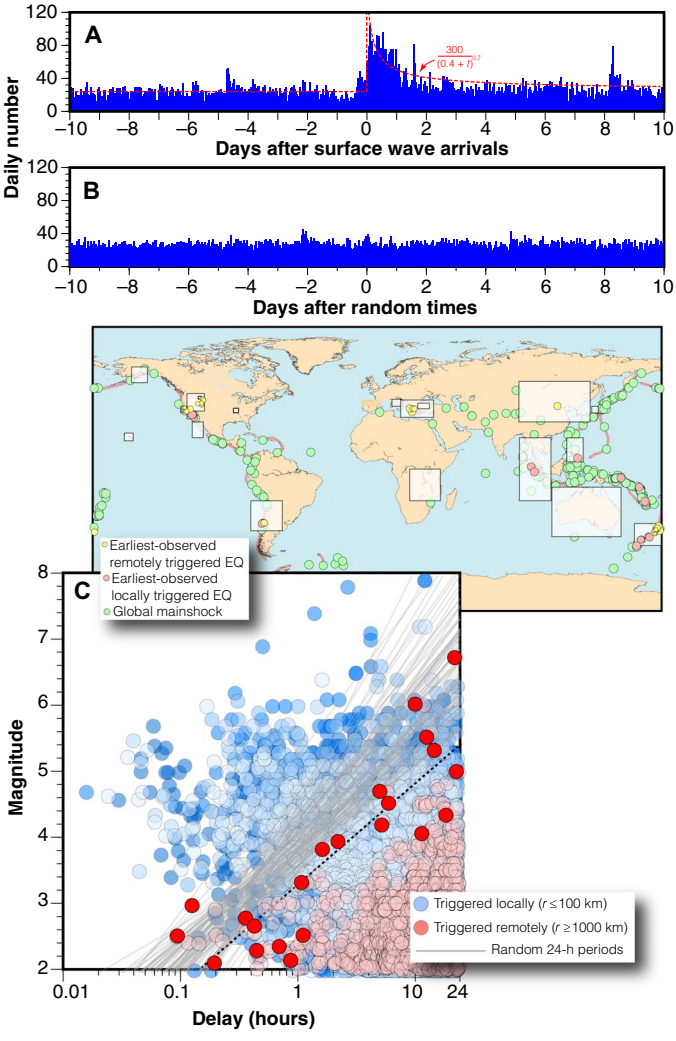

Fig. 3. (**A**) Remotely triggered earthquakes (EQ) are part of a typical Omori law time decay that is similar to local aftershocks, which suggests that their timing should be advanced relative to a random process. The remotely triggered earthquake catalog was developed from 24-hour periods following 260 $M \geq 7.0$ global mainshocks as recorded in 17 different seismograph networks around the world (white boxes on the map) (*5*). (**B**) Earthquakes from 38 randomly drawn 24-hour periods when no global or local mainshocks occurred demonstrate the anomalous nature of the rate increase associated with surface wave arrivals from global mainshocks (A). We use 38 24-hour periods because the observed data were triggered by 38 global mainshocks. (**C**) Locally ($r \leq 300$ km) (blue dots) and remotely ($r > 1000$ km) (red dots) triggered earthquakes are plotted as a function of their magnitudes. Different shading of the locally triggered events represents five realizations of nonoverlapping sample sizes equal to the remotely triggered population. First-observed remotely triggered events in 0.1 magnitude-unit bins are plotted as bright red dots. There is an evident log-linear trend of delay time versus magnitude that is less evident in the locally triggered earthquakes (histogram in Fig. 1E shows the magnitude-frequency distribution of remotely triggered earthquakes). Lines fit to first-occurrence distributions from 100 sets of 38 random 24-hour periods within the 17 local networks are shown and are all earlier than, or overlap, the remotely triggered events.

We find that a global population of remotely triggered earthquakes obeys a power-law relationship between nucleation time and magnitude and can be fit to a linear trend between magnitude and $\log_{10}$ of occurrence time (Fig. 3). Such a trend might be expected because high-magnitude earthquakes happen less often than smaller ones, and they obey an empirical power-law relationship between frequency and magnitude called the Gutenberg-Richter relation, where the number (N) of earthquakes is distributed as $\log N = a - bM$, where a is the number of events at magnitude completeness and b is observed to be ~1.0. Therefore, over extended periods and/or across large areas, an approximately 10-fold decrease in event rates is observed at each increasing magnitude-unit threshold. Thus, if we think of short-term (24 hours) earthquake occurrence in the absence of a local or remote perturbing event as steady state with randomly distributed interevent times (Poisson process), we would expect longer wait times between higher-magnitude earthquakes, and the odds of seeing higher-magnitude events in 24 hours would be lower. This means that random earthquake first-occurrence times should also follow a log-linear trend versus magnitude. Virtually every aspect of earthquake scaling (rupture area, magnitude, frequency, slip, etc.) is described by power-law relationships.

We compare observed dynamically triggered initiation times to steady-state, spontaneous earthquake occurrence. The catalog of remotely triggered earthquakes that we work with was prompted by 38 $M \geq 7$ global mainshocks out of 260 candidates, with the remaining ones having no effect. We thus examine 100 sets of 38 random 24-hour periods drawn from the same local networks when no local or global $M \geq 7$ mainshocks have happened. We follow the same procedure of binning by magnitude and finding earliest occurrences, which, as expected, also follow log-linear trends (fits shown in Fig. 3). However, they tend to happen with less delay over much of the magnitude range. Comparison between the full ranges of first-observed remotely triggered earthquake times and those from random periods using a Kolmogorov-Smirnov test [a standard approach to comparing power-law distributions (*32*)] shows virtually no overlap between the groups ($P \leq 0.01$ in 94 of 100 cases, and all cases have $P \leq 0.05$). There is correspondence between some individual first-observed remotely triggered earthquake times and random trends because all triggered sequences must contain some random background events unless pre-mainshock rates are zero. We emphasize that the comparison is made with the earliest possible nucleation times, whereas the rest of the remotely triggered events occur even later (Fig. 3). Thus, although there are significantly more earthquakes happening during the first 24 hours after surface waves pass through local networks, they are not nucleating sooner than would be expected under a random process.

We assemble a catalog of locally triggered earthquakes culled from the same 17 networks as the remotely triggered population that happened within 300 km from, and 24 hours after, $M \geq 7$ mainshocks within the networks. This catalog has more $M \geq 2$ events in it (7741 triggered by 96 $M \geq 7$ mainshocks) than the remotely triggered catalog (1249) and is likely deficient at smaller magnitudes at the earliest times because local networks become overwhelmed by the large number of aftershocks occurring simultaneously. We thus draw groups of 1249 nonoverlapping events from the full population of locally triggered earthquakes (five examples are plotted in Fig. 3) to directly compare their characteristics. Each of these groups of local

aftershocks has $M \geq 5$ events with delay times on the order of seconds to minutes, whereas the first-observed remotely triggered $M \geq 5$ earthquake is delayed by 9.85 hours.

Locally and remotely triggered aftershocks share a characteristic Omori law rate increase and exponential decay with time (Fig. 4). Fitting Omori law parameters to the observed combined global rate increase of remotely triggered earthquakes and integrating yield an expected 56% probability increase of seeing earthquakes in the 24 hours after surface wave arrivals, yet unlike locally triggered aftershocks, these event times are not advanced relative to a random process (Fig. 3). Instead, the remotely triggered shocks display a magnitude proportional delay, which is a feature unique to them.

Global observations thus identify three distinct initiation-time versus magnitude behaviors during the initial 24-hour periods. Local aftershocks are clearly advanced in time relative to earliest-observed spontaneous earthquakes in randomized 24-hour periods, which, in turn, are distinct from, but can overlap, first-observed times in the population of remotely triggered earthquakes at lower magnitudes [up to $M \sim 3$ (Fig. 3)]. However, earliest-observed higher-magnitude remotely triggered shocks are delayed relative to periods when there is no local or remote mainshock. This observation is puzzling because the overall rates of earthquakes during the 24-hour periods following surface wave arrivals are higher (compare Fig. 3A with Fig. 3B). Further, no remotely triggered events ever violate the observed magnitude-dependent nucleation speed limit (Fig. 3C) despite being part of an anomalous rate increase. We concentrate on the specific earliest occurring remotely triggered earthquakes because a systematic minimum delay time is diagnostic of the earthquake initiation (nucleation) process.

Explanation of magnitude-dependent nucleation delay

There are a number of suggested mechanisms by which delayed dynamic earthquake triggering can happen (*23*–*25*), although these apply to nucleation of all magnitudes. The exception is induced (*26*) high-pressure fluid infiltration (p) that presses open fault walls (*33*) and reduces the clamping normal stress (σ_n) that usually keeps a fault closed and locked. This can be described as Coulomb failure as $\tau = \tau_0 - \mu_s(\sigma_n - p)$, where failure stress ($\tau$) is balanced between a driving shear stress (τ_0), and the normal (clamping) stress as modified by pore pressure, and the fault friction coefficient (μ_s). Strength is reduced when pore fluid pressure increases. The reason that an induced pore fluid pressurization model is most consistent with observations is that the concept involves dynamic stressing from seismic waves disrupting a physical seal that had previously blocked free flow of fluids into a fault zone. This newly broken seal (or seals) could exist at a very specific location, and therefore, all invading fluids would have to pass through to flow into the fault zone before they can strongly influence its stress state (*26*). Thus, time is required before failure conditions are met.

Earthquake seismic moment is directly proportional to fault rupture area (*34*), meaning that a longer fluid transit time is needed to induce a larger earthquake. Rupture-area dimensions (diameter of circular rupture) range from ~0.2 to ~20 km (*35*) over the magnitude range (M = 2.0 to M = 6.7) of our observed (*5*) triggered earthquakes, marking approximate transit distances for whole rupture zones to be infiltrated. However, magnitudes also scale with the size of the smaller sticking area (asperity) that primarily resists slip and where most earthquakes begin (*36*). The critical nucleation dimension ($2L_c$ in meters) for an earthquake with seismic moment m_0 (energy release proportional to magnitude in Newton meters) is derived (*37*) as $2L_c \sim \sqrt[3]{m_0 \times 10^{-9}}$, and measures ~5 m to 2.3 km for a magnitude range between M = 2.0 and M = 6.7. This is the size of the asperity nucleation zone that must be unlocked for a fluid pressure–induced earthquake of a given magnitude to occur and represents a minimum fluid transit distance. Causative seismic waves traveling global distances have long wavelengths that simultaneously affect regions at 10^1- to 10^2-km scales, meaning that direct triggering by seismic waves involves simultaneous deformation of entire rupture areas (particularly for $M < 5$). The systematic and spatial-area dependence in our observations shows delay variations discernable over nucleation dimension differences of just a few meters (Fig. 5) and is seen on an array of global faults, indicating a universal fluid-triggering process initiated by seismic waves.

Critically stressed (near failure) faults are the only ones observed to be hydraulically conductive (*38*) and thus most susceptible to fluid-induced triggering. Fluids moving from a highly pressurized source through a porous medium, such as fault zone rocks, exhibit diffusive behavior (*39*) that takes the form of $r = c\sqrt{Dt}$, where r is the distance from the high–fluid pressure source, c is a constant [derived in one dimension for fault zones as c = 2.32 (*40*)], t is time, and D is the coefficient of diffusivity. We note the consistency between diffusion rate curves calculated with typical (*41*–*45*) fault zone diffusivity values and

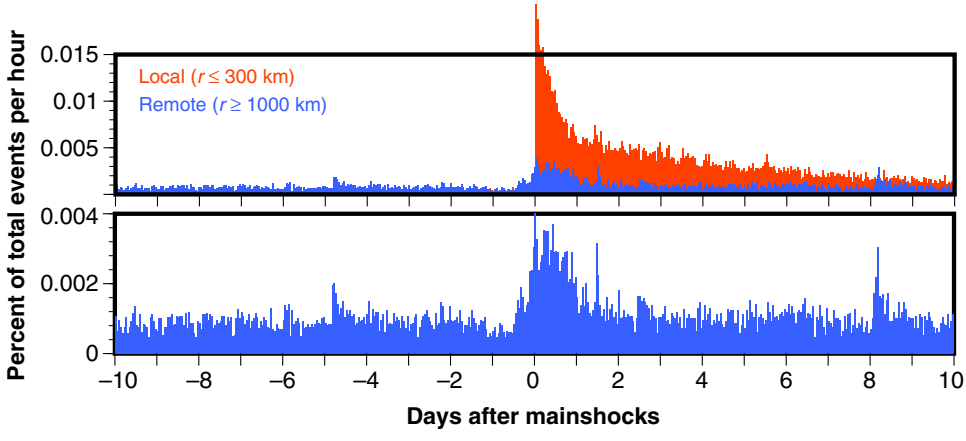

Fig. 4. Comparison between locally ($r \leq 300$ km; red) and remotely ($r \geq 1000$ km; blue) triggered earthquakes versus time. Event rates are normalized and expressed as a percentage (per hour) of the total number in the ±10-day periods. The local mainshocks produce far more aftershocks than the remote mainshocks, which is evident when they are plotted on the same scale. Both sequences display Omori law rate increases that are followed by an inverse time decay.

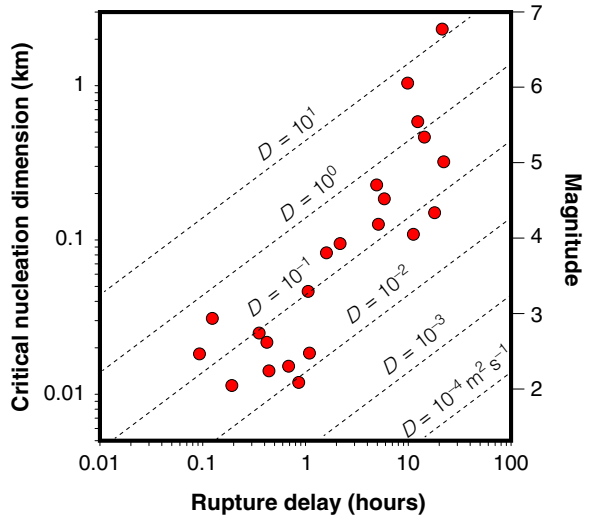

Fig. 5. Nucleation dimension–dependent delay of remotely triggered earthquakes. First-observed earthquake times versus magnitude are also plotted against their magnitude-dependent, critical nucleation dimensions. These areas are the stuck patches (asperities) of earthquakes that must become unlocked for ruptures to occur (*36*, *37*). Fault zone fluid pressurization rates are plotted for the range of observed (*41*–*45*) fault zone diffusivity values, which illustrate consistency between delay times and asperity sizes. Generally, to obtain the earliest high-magnitude (largest rupture areas) induced earthquakes, fault zones must be highly diffusive.

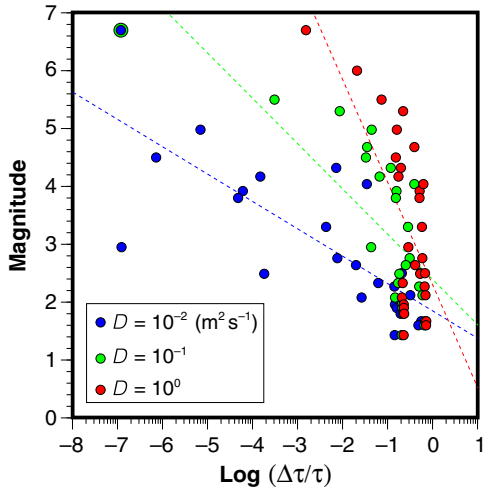

Fig. 6. Calculated pore fluid pressure induced strength reduction as a function of earthquake magnitude and fault diffusivity. Points correspond to earliest-observed remotely triggered earthquakes in Figs. 2 and 3. Strength reduction is normalized by the initial shear strength on faults, which removes nucleation depth dependence. Low-magnitude (M < 3) earthquakes can show significant reduction (10 to 100% of initial resisting shear strength) regardless of diffusivity because the rupture areas are small. Higher-magnitude triggering appears to require high diffusivity, with D approaching 1.0 m^2 s^{-1}.

observed magnitude-dependent delay expressed as time versus critical nucleation dimension (*37*) (Fig. 5). Thus, nucleation time is considered as a function of this distance and the diffusivity within the fault zone (Fig. 5). Diffusion delays can be fit to full rupture areas rather than to the smaller nucleation zones, but this requires unrealistically high (~10^2 m^2 s^{-1}) values of D.

We model induced triggering by calculating the reduction in normal (clamping) stress caused by fluid pressure infiltration into a fault zone after a sudden opening of a fault valve (*27*). If we assume initially hydrostatic conditions within target faults (pore fluid pressure equal to 0.37 of lithostatic; for an average rock density of 2.7 × 10^3 kg/m^3) and a typical fault orientation of 30° to the maximum principal stress axis, then we can calculate the frictional strength reduction resulting from the sudden opening of a moderately pressurized (pore fluid pressure, 0.6 of lithostatic) fluid compartment adjacent to the asperity. Strength reduction is a function of time, distance, and diffusivity such that a more permeable, highly diffusive fault will allow more pressure to build in a given time and distance. In other words, the speed limit on nucleation of large induced earthquakes is enforced by how fast pressurized fluids can move through a fault zone. To illustrate this, we calculate expected clamping stress reductions for observed delays of remotely triggered earthquakes over a range of diffusivity values (bracketed by measured values) (*41*–*45*) because each of the earliest-observed remotely triggered events for a given magnitude range occurred on a different fault (Fig. 3); these faults could have different diffusivity characteristics. We note for low-magnitude earthquakes (M = 2 to M = 3) that the calculated clamping stress reductions are insensitive to diffusivity because of their small nucleation zones and rupture areas (Fig. 6). For larger triggered earthquakes, our calculations show that diffusivity values on the higher end of the observed range (D ~ 10^0 m^2 s^{-1}) are required for significant clamping stress reductions, which may explain why high-magnitude remotely triggered earthquakes are rare (*5*).

DISCUSSION AND CONCLUSIONS

We find significant variation in the temporal distribution of triggered earthquakes depending on whether they are prompted by local or remote mainshocks. Both locally and remotely triggered earthquakes exhibit rate increases during the first 24 hours after they are initiated by either static or dynamic stress changes. However, only locally triggered, higher-magnitude aftershocks are advanced in time across the magnitude spectrum as compared to normal background rates.

Delayed dynamic triggering has been explained by different stress threshold models, though all but one lack a clear indication why a power-law relationship between nucleation time and magnitude should persist. A primary clue comes from the fact that earthquake rupture areas and the size of locked asperity zones scale logarithmically with magnitude. Thus, a mechanism wherein the locked part of the fault must be traversed before it ruptures suggests itself. We show that a diffusion process where shaking from passing surface waves opens up pathways between locked faults and sealed pockets of pressurized fluids is consistent with observations of nucleation delays that are proportional to magnitude.

Our results have ramifications for human-induced seismicity because conditions required for higher-magnitude triggering are potentially identifiable. Asperity identification and location are possible using advanced crustal imaging and analysis of microearthquake behavior (*46*–*49*); thus, larger critical nucleation zones might be delimited and avoided. Additionally, it is clear that the interplay between absolute stress, fluid pressure, and fault zone diffusivity (a measurable quantity) governs the occurrence and timing of induced earthquakes of a given magnitude.

METHODS

The catalog of remotely triggered earthquakes was compiled in a previous study (*5*), and we briefly describe how it was developed. Daily changes in the number of earthquakes in each regional catalog were calculated over their durations (typically two to three decades) excluding the 260

24-hour periods after global mainshocks occurred. Mean daily changes (δ) and variances are found in 2-year sliding time windows at 0.5-year intervals because catalogs grow more complete and record more events with time. Time-dependent variance and SDs (σ) were found by fitting daily rate changes to negative binomial distributions, which represent clustered phenomena (*50*, *51*). A maximum likelihood regression technique (*52*) was iterated until the change in the log likelihood was vanishingly small, yielding the dispersion (temporal clustering factor α) inherent to each catalog. Time-dependent variance for each catalog was calculated as $\mathrm{var}(t) = \delta + \alpha\delta^2$ to find 1σ and 2σ variations. One-day periods following 260 $M \geq 7$ mainshocks were then examined for significant (>2σ) rate increases in all regional networks. Mainshocks closer than 1000 km were excluded to remove any possibility that local static stress change–induced processes could be mistaken for remote triggering. Every significant rate increase was examined in detail to establish its character. A significant regional outbreak of triggered earthquakes was quantified by first dividing network regions into 0.5° × 0.5° boxes and then calculating the means and variances of each with 100 random trials across catalog durations. If the number of affected subregions after a global mainshock exceeded a 2σ threshold in the number from random trials, and there was no local mainshock, then we identified the response as widespread and, thus, probable remote triggering. Earliest-observed remotely triggered earthquakes versus magnitude were found by subtracting surface wave travel times between source mainshock and remote events and sorting into time order within 0.1 magnitude-unit bins. If there were a possibility that an earliest-observed event could be a local aftershock, based on proximity to a preceding earthquake, it was excluded.

We calculated *b* values (slopes of magnitude-frequency distributions) using the maximum likelihood method (*53*, *54*), which uses the equation $b = \frac{1}{\bar{M} - \mathrm{M_{min}}} \log e$, where $\bar{M}$ is the mean magnitude and M_{min} is the minimum magnitude. The SE can be calculated (*55*) using $\sigma(b) = 2.30b^2\sigma(\bar{M})$, where

$$\sigma^2(\bar{M}) = \sum_{i=1}^{n} \frac{(M_i - \bar{M})^2}{n(n-1)}$$

We report 95% confidence bounds on the calculations. A higher *b* value indicates a distribution that lacks higher-magnitude events relative to lower values.

We modeled strength reduction

$$\begin{cases} \Delta\tau = \mu_s \ [(\sigma_n - P_{\mathrm{FINAL}}) - (\sigma_n - P_{\mathrm{INITIAL}})] = \mu_s \Delta P \\ \Delta P = P_{\mathrm{INITIAL}} - P_{\mathrm{FINAL}} \end{cases}$$

from fluid pressurization within the observed delay times and rupture sizes. The initial stress states of normal, reverse, and strike-slip faults may be written as (*40*)

$$\begin{cases} \sigma_n = \dfrac{g\ z\ \rho_r(1-\lambda_f)\ \sin(\theta)}{\mu_s \cos(\theta) + \sin(\theta)} \\ \tau_y = \mu_s \sigma_n \end{cases}, \quad \begin{cases} \sigma_n = \dfrac{g\ z\ \rho_r(1-\lambda_f)\ \cos(\theta)}{\cos(\theta) - \mu_s\ \sin(\theta)} \\ \tau_y = \mu_s \sigma_n \end{cases},$$

$$\begin{cases} \sigma_n = \dfrac{g\ z\ \rho_r\ (1-\lambda_f)\ \sin(2\theta)}{\mu_s\ \cos(2\theta) + \sin(2\theta)} \\ \tau_y = \mu_s \sigma_n \end{cases}$$

where θ is the angle between the fault plane and the maximum principal stress axis (assumed to be 30°), and μ_s is the fault friction coefficient (assumed to be 0.6). Shear stress τ represents the strength of a fault, which is highest at minimum pore fluid pressures (hydrostatic). We assumed that the volumes where triggered earthquakes occur were originally under hydrostatic conditions ($\lambda_f \approx 0.37$) and that an overpressured, initially sealed crustal compartment ($\lambda_f \approx 0.6$) was located adjacent to nucleation. The purpose of the calculations is to demonstrate functional consistency between nucleation delay times and failure stress increase; thus, although values are sensitive to parameter choices, the logarithmic form of delay times is not. For the one-dimensional problem of two half-spaces in contact, in which the overpressure remains constant over time, after seismic waves break the seal, fault pore fluid pressure increases with time and distance as

$$P(x,t) = (P_0 - P_1)erf\left(\frac{x}{2\sqrt{Dt}}\right) + P_1$$

where

$$\begin{cases} P(x=0, t>0) = P_0 = \lambda_f \rho_r g z \\ P(x>0, t=0) = P_1 = \rho_w g z \end{cases}$$

with ρ_r as rock density and ρ_w as water density. P_0 is the overpressure, and P_1 is the hydrostatic pressure.

REFERENCES AND NOTES

1. R. S. Stein, The role of stress transfer in earthquake occurrence. *Nature* **402**, 605–609 (1999).
2. D. P. Hill, S. Prejean, in *Earthquake Seismology*. *Treatise on Geophysics*, H. Kanamori, G. Schubert, Eds. (Elsevier, ed. 2, 2015), vol. 4, pp. 273–304.
3. A. A. Velasco, S. Hernandez, T. Parsons, K. Pankow, Global ubiquity of dynamic earthquake triggering. *Nat. Geosci.* **1**, 375–379 (2008).
4. T. Parsons, Global Omori law decay of triggered earthquakes: Large aftershocks outside the classical aftershock zone. *J. Geophys. Res.* **107**, 2199 (2002).
5. T. Parsons, M. Segou, W. Marzocchi, The global aftershock zone. *Tectonophysics* **618**, 1–34 (2014).
6. S. G. Prejean D. P. Hill, E. E. Brodsky, S. E. Hough, M. J. S. Johnston, S. D. Malone, D. H. Oppenheimer, A. M. Pitt, K. B. Richards-Dinger, Remotely triggered seismicity on the United States west coast following the M_w 7.9 Denali Fault earthquake. *B. Seismol. Soc. Am.* **94**, S348–S359 (2004).
7. D. P. Hill, P. A. Reasenberg, A. Michael, W. J. Arabaz, G. Beroza, D. Brumbaugh, J. N. Brune, R. Castro, S. Davis, D. dePolo, W. L. Ellsworth, J. Gomberg, S. Harmsen, L. House, S. M. Jackson, M. J. S. Johnston, L. Jones, R. Keller, S. Malone, L. Munguia, S. Nava, J. C. Pechmann, A. Sanford, R. W. Simpson, R. B. Smith, M. Stark, M. Stickney, A. Vidal, S. Walter, V. Wong, J. Zollweg, Seismicity remotely triggered by the magnitude 7.3 Landers, California, earthquake. *Science* **260**, 1617–1623 (1993).
8. D. Kilb, J. Gomberg, P. Bodin, Triggering of earthquake aftershocks by dynamic stresses. *Nature* **408**, 570–574 (2000).
9. H. M. Savage, C. Marone, Potential for earthquake triggering from transient deformations. *J. Geophys. Res.* **113**, B05302 (2008).
10. E. A. Roeloffs, Persistent water level changes in a well near Parkfield, California, due to local and distant earthquakes. *J. Geophys. Res.* **103**, 869–889 (1998).
11. M. Weingarten, S. Ge, Insights into water level response to seismic waves: A 24 year high-fidelity record of global seismicity at Devils Hole. *Geophys. Res. Lett.* **41**, 74–80 (2014).
12. M. Miyazawa, J. Mori, Evidence suggesting fluid flow beneath Japan due to periodic seismic triggering from the 2004 Sumatra-Andaman earthquake. *Geophys. Res. Lett.* **33**, L05303 (2006).
13. M. Manga, E. Brodsky, Seismic triggering of eruptions in the far field: Volcanoes and geysers. *Annu. Rev. Earth Planet. Sci.* **34**, 263–291 (2006).
14. A Cannata, G. Di Grazia, P. Montalto, M. Aliotta, D. Patanè, E. Boschi, Response of Mount Etna to dynamic stresses from distant earthquakes. *J. Geophys. Res.* **115**, B12304 (2010).
15. Z. Peng, J. E. Vidale, A. G. Wech, R. M. Nadeau, K. C. Creager, Remote triggering of tremor along the San Andreas fault in central California. *J. Geophys. Res.* **114**, B00A06 (2009).

16. D. P. Hill, Z. Peng, D. R. Shelly, C. Aiken, *S*-wave triggering of tremor beneath the Parkfield, California, section of the San Andreas Fault by the 2011 Tohoku, Japan earthquake: Observations and theory. *Bull. Seismol. Soc. Am.* **103**, 1541–1550 (2013).
17. L. Linville, K. Pankow, D. Kilb, A. Velasco, Exploring remote earthquake triggering potential across EarthScopes' Transportable Array through frequency domain array visualization. *J. Geophys. Res.* **119**, 8950–8963 (2014).
18. C. W. Johnson, R. Bürgmann, Delayed dynamic triggering: Local seismicity leading up to three remote $M \geq 6$ aftershocks of the 11 April 2012 M8.6 Indian Ocean earthquake. *J. Geophys. Res.* **121**, 134–151 (2016).
19. C. W. Johnson, R. Bürgmann, F. F. Pollitz, Rare dynamic triggering of remote $M \geq 5.5$ earthquakes from global catalog analysis. *J. Geophys. Res.* **120**, 1748–1761 (2015).
20. R. R. Castro, H. González-Huízar, F. R. Zúñiga, V. N. Wong, A. A. Velasco, Delayed dynamic triggered seismicity in northern Baja California, México caused by large and remote earthquakes. *B. Seismol. Soc. Am.* **105**, 1825–1835 (2015).
21. F. F. Pollitz, R. S. Stein, V. Sevilgen, R. Bürgmann, The 11 April 2012 east Indian Ocean earthquake triggered large aftershocks worldwide. *Nature* **490**, 250–253 (2012).
22. T. Parsons, A. A. Velasco, Absence of remotely triggered large earthquakes beyond the mainshock region. *Nat. Geosci.* **4**, 312–316 (2011).
23. Z. Peng, C. Wu, C. Aiken, Delayed triggering of microearthquakes by multiple surface waves circling the Earth. *Geophys. Res. Lett.* **38**, L04306 (2011).
24. J. Gomberg, N. M. Beeler, M. L. Blanpied, P. Bodin, Earthquake triggering by transient and static deformations. *J. Geophys. Res.* **103**, 24411–24426 (1998).
25. T. Parsons, A hypothesis for delayed dynamic earthquake triggering. *Geophys. Res. Lett.* **32**, L04302 (2005).
26. E. E. Brodsky, E. Roeloffs, D. Woodcock, I. Gall, M. Manga, A mechanism for sustained groundwater pressure changes induced by distant earthquakes. *J. Geophys. Res.* **108**, 2390 (2003).
27. R. H. Sibson, in *Deformation Mechanisms, Rheology and Tectonics*, R. J. Knipe, E. H. Rutter, Eds. (Geological Society of London Special Publications, 1990), pp. 15–28.
28. K. L. Pankow, W. J. Arabasz, J. C. Pechmann, S. J. Nava, Triggered seismicity in Utah from the 3 November 2002 Denali fault earthquake. *B. Seismol. Soc. Am.* **94**, S332–S347 (2004).
29. H. Gonzalez-Huizar, A. A. Velasco, Dynamic triggering: Stress modeling and a case study. *J. Geophys. Res.* **116**, B02304 (2011).
30. D. P. Hill, Dynamic stresses, Coulomb failure, and remote triggering. *B. Seismol. Soc. Am.* **98**, 66–92 (2008).
31. F. Omori, "On aftershocks" (Report of Imperial Earthquake Investigation Committee, 1894).
32. A. Clauset, C. R. Shalizi, M. E. J. Newman, Power-law distributions in empirical data. *SIAM Rev.* **51**, 661–703 (2009).
33. K. Terzaghi, Die berechnung des durchlassigkeitsziffer des tones aus dem verlauf der hydrodynamischen spannungserscheinungen. *Sitz. Akad. Wiss. Wien* **132**, 125–138 (1923).
34. H. Kanamori, The energy release in great earthquakes. *J. Geophys. Res.* **82**, 2981–2987 (1977).
35. D. L. Wells, K. J. Coppersmith, New empirical relationships among magnitude, rupture length, rupture width, rupture area, and surface displacement. *B. Seismol. Soc. Am.* **84**, 974–1002 (1994).
36. T. Lay, H. Kanamori, An asperity model of large earthquake sequences, in *Earthquake Prediction—An International Review*, D. W. Simpson, P. G. Richards, Eds. (American Geophysical Union, 1981), pp. 579–592.
37. M. Ohnaka, A physical scaling relation between the size of an earthquake and its nucleation zone size. *Pure Appl. Geophys.* **157**, 2259–2282 (2000).
38. C. A. Barton, M. D. Zoback, D. Moos, Fluid flow along potentially active faults in crystalline rock. *Geology* **23**, 683–686 (1995).
39. A. Fick, V. On liquid diffusion. *Philos. Mag.* **10**, 30–39 (1855).
40. L. Malagnini, F. P. Lucente, P. De Gori, A. Akinci, I. Munafo, Control of pore fluid pressure diffusion on fault failure mode: Insights from the 2009 L'Aquila seismic sequence. *J. Geophys. Res.* **117** (2012).
41. W. Tanikawa, H. Mukoyoshi, W. Lin, T. Hirose, A. Tsutsumi, Pressure dependence of fluid transport properties of shallow fault systems in the Nankai subduction zone. *Earth, Planets Space* **66**, 90 (2014).
42. A. Rigo, Precursors and fluid flows in the case of the 1996, M_L = 5.2 Saint-Paul-de-Fenouillet earthquake (Pyrenees, France): A complete pre-, co- and post-seismic scenario. *Tectonophysics* **480**, 109–118 (2010).
43. S. Bourouis, F. H. Cornet, Microseismic activity and fluid fault interactions: Some results from the Corinth Rift Laboratory (CRL), Greece. *Geophys. J. Int.* **178**, 561–580 (2009).
44. S. A. Shapiro, J. Kummerow, C. Dinske, G. Asch, E. Rothert, J. Erzinger, H.-J. Kümpel, R. Kind, Fluid induced seismicity guided by a continental fault: Injection experiment of 2004/2005 at the German Deep Drilling Site (KTB). *Geophys. Res. Lett.* **33**, L01309 (2006).
45. M. L. Doan, E. E. Brodsky, Y. Kano, K. F. Ma, In situ measurement of the hydraulic diffusivity of the active Chelungpu Fault, Taiwan. *Geophys. Res. Lett.* **33**, L16317 (2006).
46. Y. Font, M. Segovia, S. Vaca, T. Theunissen, Seismicity patterns along the Ecuadorian subduction zone: New constraints from earthquake location in a 3-D a priori velocity model. *Geophys. J. Int.* **193**, 263–286 (2013).
47. S. Y. Schwartz, J. W. Dewey, T. Lay, Influence of fault plane heterogeneity on the seismic behavior in the southern Kurile Islands Arc. *J. Geophys. Res.* **94**, 5637–5649 (1989).
48. T. Tormann, S. Wiemer, S. A. Mignan, A systematic survey of high-resolution *b* value imaging along Californian faults: Inference on asperities. *J. Geophys. Res.* **119**, 2029–2054 (2014).
49. T. H. W. Goebel, T. W. Becker, D. Schorlemmer, S. Stanchits, C. Sammis, E. Rybacki, G. Dresen, Identifying fault heterogeneity through mapping spatial anomalies in acoustic emission statistics. *J. Geophys. Res.* **117**, B03310 (2012).
50. D. Vere-Jones, Stochastic models for earthquake occurrence. *J. R. Stat. Soc. B* **32**, 1–62 (1970).
51. D. D. Jackson, Y. Y. Kagan, Testable earthquake forecasts for 1999. *Seism. Res. Lett.* **70**, 393–403 (1999).
52. A. C. Cameron, P. K. Trivedi, *Regression Analysis of Count Data, Econometric Society Monograph No. 30* (Cambridge Univ. Press, 1998).
53. K. Aki, Maximum likelihood estimate of *b* in the formula log $N = a - bM$ and its confidence limits. *Bull. Earthquake Res. Inst. Univ. Tokyo* **43**, 237–239 (1965).
54. T. Utsu, A method for determining the value of *b* in a formula log $n = a - bM$ showing the magnitude-frequency relation for earthquakes. *Geophys. Bull. Hokkaido Univ.* **13**, 99–103 (1965).
55. Y. Shi, B. A. Bolt, The standard error of the magnitude-frequency *b* value. *B. Seismol. Soc. Am.* **72**, 1677–1687 (1982).

Acknowledgments: T.P. thanks the INGV (Istituto Nazionale di Geofisica e Vulcanologia) for a hospitable and productive visit. We thank G. Beroza and two anonymous reviewers for their helpful comments and their time. **Funding:** The authors received no external funding for the research presented in this paper. **Author contributions:** T.P. wrote part of the manuscript, analyzed the earthquake catalog data, created figures, and conducted statistical analyses. L.M. and A.A. conceived and calculated fault strength reduction from fluid pressurization models, created figures, and wrote part of the manuscript. **Competing interests:** The authors declare that they have no competing interests. **Data and materials availability:** All data needed to evaluate the conclusions in the paper are present in the paper. Additional data related to this paper may be requested from the authors. Earthquake catalog data may be requested from the Advanced National Seismic System and Global Seismographic Network.

Submitted 6 March 2017
Accepted 1 August 2017
Published 23 August 2017
10.1126/sciadv.1700660

Citation: T. Parsons, L. Malagnini, A. Akinci, Nucleation speed limit on remote fluid-induced earthquakes. *Sci. Adv.* **3**, e1700660 (2017).